



DOI: 10.29026/oea.2018.180007

# Scanning cathodoluminescence microscopy: applications in semiconductor and metallic nanostructures

Zhixin Liu<sup>†</sup>, Meiling Jiang<sup>†</sup>, Yanglin Hu, Feng Lin, Bo Shen, Xing Zhu, Zheyu Fang\*

Cathodoluminescence (CL) as a radiative light produced by an electron beam exciting a luminescent material, has been widely used in imaging and spectroscopic detection of semiconductor, mineral and biological samples with an ultrahigh spatial resolution. Conventional CL spectroscopy shows an excellent performance in characterization of traditional material luminescence, such as spatial composition variations and fluorescent displays. With the development of nanotechnology, advances of modern microscopy enable CL technique to obtain deep valuable insight of the testing sample, and further extend its applications in the material science, especially for opto-electronic investigations at nanoscale. In this article, we review the study of CL microscopy applied in semiconductor nanostructures for the dislocation, carrier diffusion, band structure, doping level and exciton recombination. Then advantages of CL in revealing and manipulating surface plasmon resonances of metallic nanoantennas are discussed. Finally, the challenge of CL technology is summarized, and potential CL applications for the future opto-electronic study are proposed.

**Keywords:** cathodoluminescence; microscopy; semiconductor; metallic nanostructures; surface plasmons

Liu Z X, Jiang M L, Hu Y L, Lin F, Shen B *et al.* Scanning cathodoluminescence microscopy: applications in semiconductor and metallic nanostructures. *Opto-Electronic Advances* **1**, 180007 (2018).

## Introduction

Cathodoluminescence (CL) as an optical and electromagnetic phenomenon referring to the radiation in a form of fluorescence<sup>1</sup>, was first discovered in the mid-nineteenth century from cathode electron rays hitting a glass substrate. When incident electrons interact with a luminescent matter, material properties make a difference in CL spectra. As the development of nanotechnology and nanoscience, the demand for high-resolution microscopy and characterization techniques has tremendously increased. In addition to traditional optical measurements, the scanning near-field optical microscopy (SNOM) presents a higher spatial resolution<sup>2</sup>, but suffers from an unavoidable interaction between the scanning probe and the material surface. CL microscopy, on the other side, providing a label-free optical imaging technique with deep subwavelength resolution, has achieved significant interests for the mineralogy<sup>3-5</sup>, semiconductor physics<sup>6-8</sup>, and many other research fields like the tracking of cellular processes in biology<sup>9,10</sup>. CL was also found extensive applications as

the emission source in cathode-ray-tube computer monitors and televisions for the industry.

CL spectroscopy is usually operated in scanning electron microscopy (SEM)<sup>11</sup>, although it is also possible to perform measurements in transmission electron microscopy (TEM) and scanning transmission electron microscopy (STEM)<sup>12</sup>. When the focused electron beam passes through the aperture hole of the parabolic mirror and hits on the sample surface, CL generated from the luminescent material can be reflected by the mirror and collected by photomultiplier tube (PMT) or a charge-coupled device (CCD) where CL images can be obtained. Another case is that CL is directly received by CCD instead of converging through lens. The system can interpret the radiation angle distribution of the sample according to the CCD image, since the light signal received at different positions on the CCD reflects the light information radiated from the sample in different directions. Therefore, angle-resolved CL measurement can be realized. In addition, the system supports the use of an optical fiber to derive the CL signal and couple it to an external spectrometer (Fig. 1). The spectrometer is used to separate CL

School of Physics, State Key Lab for Mesoscopic Physics, Academy for Advanced Interdisciplinary Studies, Collaborative Innovation Center of Quantum Matter, Peking University, Beijing 100871, China

<sup>†</sup>These authors contributed equally to this work.

\*Correspondence: Z Y Fang, E-mail: zhyfang@pku.edu.cn

Received 17 April 2018; accepted 24 June 2018; accepted article preview online 29 June 2018

180007-1

emissions in different wavelength ranges and benefit the spectral analysis. The mineral composition<sup>13</sup>, band structure<sup>14-16</sup> and impurity defects of the material<sup>17-19</sup> can be effectively inferred by the observed CL intensity, wavelength range and the degree of light polarization.

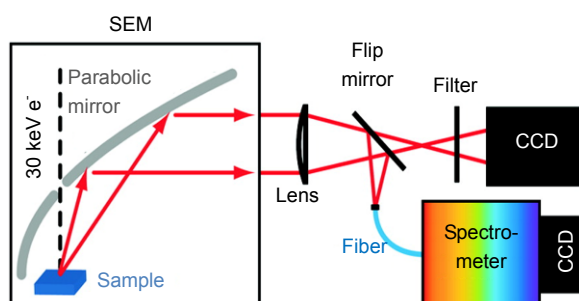


**Fig. 1 | Schematic overview of a CL imaging spectrometer with spectral analysis function.** Figure reproduced from ref. <sup>11</sup>, CUP Publishing.

Cherenkov and transition radiations are two of main direct emission processes that involved in CL, which are coherent with the external field of the incoming electron, as all of the electromagnetic fields are described by the same set of Maxwell's equations. Incoherent emission is generally associated with electron-hole recombination in semiconductors which is stronger and does not interfere with coherent radiation. Generally, these two radiation mechanisms can be distinguished by their characteristic angle profiles, dipolar-like lobes for transition radiation and a lambertian angular distribution for incoherent luminescence<sup>7</sup>.

Cherenkov radiation is mainly observed in semiconductors, when an electron passing through a transparent sample with its speed faster than the phase velocity of light in that medium. Transition radiation occurs during the reconstruction of the Coulomb field, when the point charge of a uniform linear motion moves in a non-uniform condition such as a medium interface. For semiconductors, CL microscopy possesses the ability of deep penetration depth and ultrahigh spatial resolution. For example, in a one-dimensional CdS nanostructure, the penetration depth of the injected electrons may reach hundreds of nanometers or even several micrometers under an accelerating voltage of 10 kV, and a nanoscale resolution is achieved in CL mapping<sup>20</sup>. The optical behavior of different depths of material can be detected at various accelerating voltages of the electron probe, for example, CL intensity increases as the applied voltage changes from 5 to 19 kV in ZnO nanobullet<sup>21</sup>. The ultrahigh spatial resolution capabilities of CL microscopy can be used to analyze the distribution of surface dislocations, the property of material band structures, and the optical emission of quantum dots<sup>22-23</sup>. Recently, CL microscopy has been also successfully applied for two-dimensional (2D) materials<sup>24</sup>, where the investigation of exciton cou-

pling was realized with a higher optical resolution.

On the other hand, transition radiation happens when an electron passes through a boundary between two media with different dielectric constants. It is created by the time dependent variation and eventual collapse of the dipole moment that generated by the incident electron and its image charge in the dielectric. This effect was predicted and observed for metals. Surface plasmons<sup>25-27</sup> (SPs), as the collective oscillation of surface electrons at the interface between dielectric and metal, have attracted huge attentions for applications like super-imaging<sup>28</sup>, nanofocusing<sup>29</sup>, waveguiding<sup>30-33</sup>, and light harvesting<sup>34</sup>. With the development of metallic nanostructures based plasmonics, CL has been widely applied for the SPs characterization, such as the light emission from the metallic grating structure<sup>35-37</sup> and nanoparticle<sup>38-40</sup> under the electron excitation. The emitted fluorescence during the plasmon coupling can be applied to the imaging of the resonance mode<sup>41,42</sup> and further realize the angle-resolved spectroscopy<sup>43,44</sup>. CL microscopy as an effective characterization method, can reflect the distribution of radiative local density of states (LDOS), which directly determine the light-matter interaction. With properly designing metallic nanostructures, it is possible to control and manipulate the light emission at deep sub-wavelength scale for future information and quantum studies.

In addition, both electron energy loss spectroscopy (EELS) and photoemission electron microscopy (PEEM) have extraordinary performance on high-resolution characterization and provide distinctive directions for investigating plasmons. EELS is an analytical method for obtaining the physical and chemical information of surface atoms by the loss of energy due to inelastic scattering of electron beams incident on the surface of the sample. It can measure dark plasmon modes and characterize dipoles and high-order modes<sup>45,46</sup>. The combination of CL microscopy and EELS to measure dark plasmon modes can compensate for the inability of EELS to distinguish plasmon radiation modes from non-radiative modes. Based on the photoelectric effect, PEEM functions on an electron microscope that images the photoelectron emission distribution of a sample surface, obtains near-field mapping and dynamic properties of plasmonic nanostructures<sup>47,48</sup>.

In this review, we focus on CL investigations for semiconductors and metallic nanostructures, respectively. In addition, CL microscopy at low-temperature, and with angle-resolved, time-resolved techniques are discussed for the modern multi-functional high-resolution characterization. In conclusion, challenges and perspectives for the future CL spectroscopy applications are presented.

## CL microscopy for semiconductors

Characterization of localized luminescence properties in semiconductors is important for the investigation of semiconductor physics and the development of

opto-electronic devices. CL microscopy with its unique features of large scanning area and short total measuring time, can be used to study any point on a sample with an electron beam. Besides, the high intensity of the incident electron beam reduces the exposure time, making CL microscopy suitable to explore the internal structure and interface dynamics of the matter.

Luminescence from a semiconductor is induced by the electron-hole pair recombination that can be generated by light or the electron beam excitation. For electron excitation, primary electrons can excite plasmons, valence electrons and inner shell electrons by losing energy. Each of these processes contributes to the generation of electron-hole pairs. Plasmons can decay into excitons, excitation of valence electrons can produce electron-hole pairs, but the excitation of secondary electrons is the main source of electron-hole pairs<sup>49</sup>. With a cascade process, the secondary electrons which have kinetic energies of 5–10 eV, can be excited and diffused in a spherical region with a depth of a few hundred nanometers for a general semiconductor under an electron beam of several keV. The electron-hole pair generated by secondary electrons recombines and further emits the luminescence, thus the spatial resolution of CL microscopy is at the level of the diffusion depth of secondary electrons.

CL microscopy has been successfully used to characterize the morphology of semiconductors, and other insightful material physics like the spatial distribution of threading dislocations<sup>50,51</sup>, length of carrier diffusions<sup>52,53</sup>, and doping level of the electric band structure<sup>54</sup>, which gives a full description of the sample.

Dislocations as the microscopic defect of crystalline semiconductors, are the local irregularity within a crystal structure. The presence of dislocations strongly influences many material properties. For example, the defect of GaP surface was characterized by the CL microscopy in a deep sub-wavelength spatial resolution, where the CL image shows black dots at the location of dislocations<sup>50</sup>. These black dots were analyzed as non-radiative recombination centers for free carriers in the semiconductor, and this non-radiative property was caused by the dislocation of the sample. Experimental results further show that different types of dislocations such as screws, edges and mixed dislocations can result CL spots with similar size and intensity. From the CL measurement, the dopant and the orientation of the crystal, dislocations grown in the epitaxial semiconductor are all non-radiative recombination centers. But in piezoelectric crystals such as GaN, uniform strain produces piezoelectric polarization, piezoelectric fields can dissociate excitons and separate the electron hole pairs<sup>55</sup>. This suggests that the carrier recombination may be inherent in the dislocation, and independent with the impurity and other point defects in the material. The beam current can affect the degree of non-radiative recombination activities in dislocations, and large beam current corresponds to the active

non-radiative recombination state as well as the large dark contrast around dislocations in CL images<sup>56</sup> (Fig. 2). Figures 2d–2f shows a significant drop in luminous efficiency due to current increase at lower magnification. This theory shows that the decrease in luminous efficiency of the white light emitting diodes (LED) can be effectively reduced by significantly reducing the dislocation density of the material.

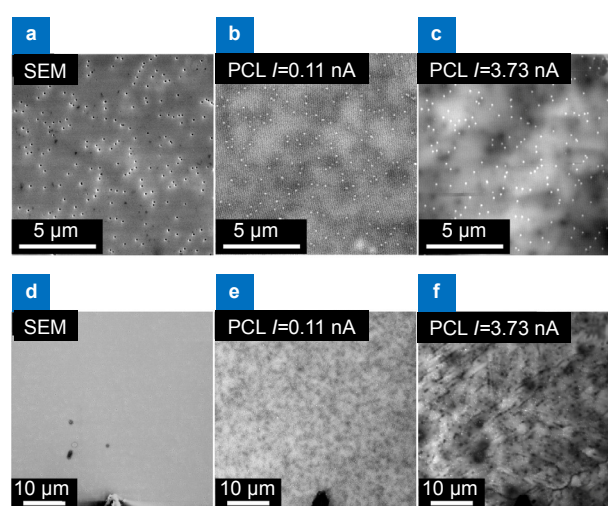


**Fig. 2** | (a) SEM image of the GaN/InGaN multiple quantum well surface. (b,c) CL image of the same area of (a) at electron beam currents of 0.11 nA and 3.73 nA, respectively. (d–f) The same images at lower magnification clearly demonstrate the decline in luminous efficiency. Figure reproduced from ref. <sup>56</sup>, AIP Publishing.

The carrier diffusion length  $L_d$  is another important factor for the semiconductor physics and light-emitting device application. CL microscopy provides an efficient way to determine the carrier and free exciton diffusion length in semiconductors<sup>57</sup>. The schematic of the measurement is shown in Fig. 3a, and the electron beam excites excess carriers of the sample through a metal mask which is opaque to the CL emission. Thus, the CL signal generated by the carrier recombination can only be obtained outside of the metal mask, and the diffusion length of excited carriers can be calculated by  $I_{CL} = I_0 e^{-x/L_d}$ , where  $I_{CL}$  and  $I_0$  represent the CL intensity measured at point  $x$  and measured at a distance  $\gg L_d$ <sup>58</sup>, respectively.  $x$  is defined as the distance between the excitation point and the edge of the metal mask. Figure 3b shows that at low temperature, because of the tunneling-assisted transport effect in conjunction with localized band-tail states, the carrier diffusion length of the InGa quantum wells strongly depends on the electron-beam current  $i_b$ . The diffusion length increases with the enhancement of the excitation electron energy, where the growth of the excited state density enlarges the tunneling probability. Thus, it is essential to study the transmission mechanism of high local density semiconductors by using CL.

Energy band transition is a vital physical process of

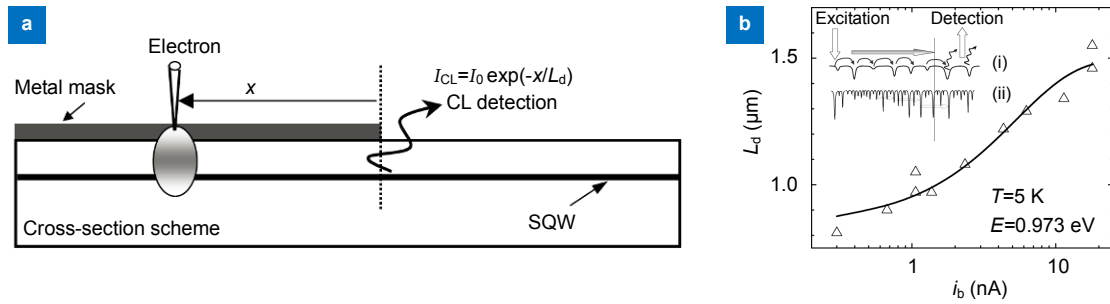


**Fig. 3 |** (a) Schematic of CL method for the measurement of  $L_d$ . (b)  $L_d$  as a function of the electron-beam current  $i_b$  at 5 K. **Inset:** Schematic of the carrier transport in conjunction with localized states for low (i) and high (ii) densities of localized states. Figure reproduced from ref. <sup>57</sup>, John Wiley & Son.

semiconductor luminescence. CL technology, as a means of deep subwavelength spatial resolution, can characterize luminescent properties of nanoscale semiconductor structures and analyze the energy band transition process. For example, CL microscopy can accurately distinguish luminescent properties at different positions of a single AlGaIn nanocolumn containing a series of GaN quantum disks at the top of the column<sup>59</sup>. The SEM images and CL images of the sample are shown in Fig. 4a. CL images contain three emission states corresponding to three detection energies in Fig. 4b, solely. Luminescence spectra of the quantum disk region and the AlGaIn region are also plotted in Fig. 4b, where the broadening of the CL1 peak with respect to the CL2 peak is mainly due to the lateral

strain distribution, change of the band-filled, inhomogeneous electric-field and variations among the quantum disks. Therefore, using CL microscopy to study energy band transitions of nanoscale semiconductor structures containing complex components is of great significance.

Doping level is a concerned physical parameter of the semiconductor, which affects its characteristic parameters such as the forbidden band width, resistivity, carrier mobility, and unbalanced carrier lifetime. The CL technique provides an effective means for measuring the local carrier concentration at the nanoscale resolution. For example, the doping level of silicon-doped GaAs semiconductor nanowires at nanometer scale has been measured by CL spectroscopy<sup>54</sup> (Fig. 5). Based on generalized Planck's law,

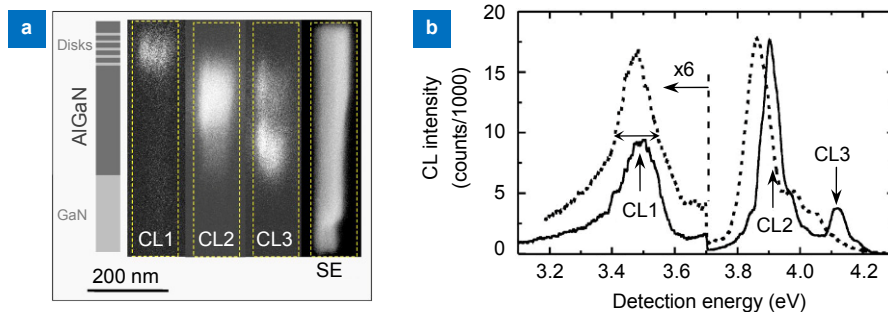


**Fig. 4 |** (a) Schematic, CL images and SEM image of the single nanocolumn. (b) CL spectra of two single GaN/AlGaIn nanocolumns. Figure reproduced from ref. <sup>59</sup>, AIP Publishing.

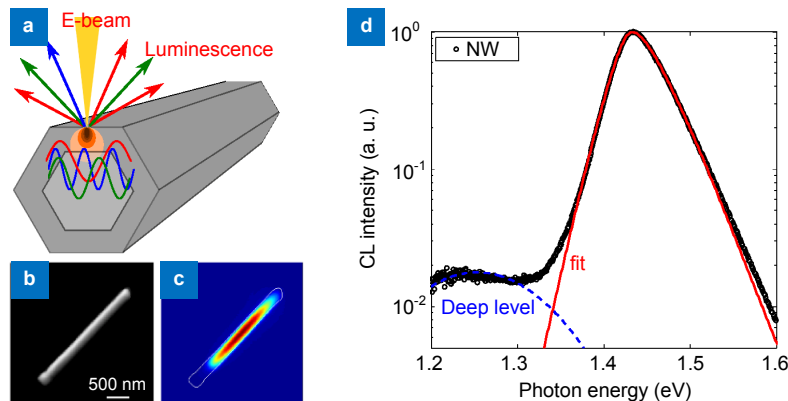


**Fig. 5 |** (a) Schematic of the electron beam interaction with nanowire and luminescence emission. (b) SEM image of a single nanowire. (c) CL image of a single GaAs nanowire measured at 30 K. (d) CL spectrum from nanowire at room temperature and the fit (red curve). Figure reproduced from ref. <sup>54</sup>, ACS Publications.

a fitting model was demonstrated to fit the CL spectrum of nanowires, in which Fermi energy could be distinguished. Experimental results indicate that the carrier concentration calibrated by Hall measurement is consistent with the one extracted from the CL spectrum (Fig. 5d). Furthermore, the influence of temperature and external field strength on the carrier concentration can also be analyzed according to CL images. This theory shows that CL microscopy provides an effective and high-resolution method for detecting the carrier concentration of semiconductor nanowires, and can also be applied to other semiconductor nanostructures with definite band structures.

The exciton effect has an essential influence on the physical processes and optical properties in semiconductors<sup>60–62</sup>. The absorption and recombination of excitons directly affect the light absorption and luminescence of semiconductors. In 2D semiconductor materials<sup>63–66</sup>, due to their low dimensionality and surface defects, the spatial resolution must be reduced to the nanometer scale in order to study exciton recombination and optical properties. However, the traditional photoluminescence is restricted at sub-nanoscale due to the diffraction limit of incident light. CL microscopy is a promising method for studying the exciton effect in 2D semiconductor materials. For 2D material systems, the electron beam can only stimulate electronic transitions in tens of nanometers range resulting that collected CL signals are weak. This problem can be effectively solved, for example, by using an hBN/WSe<sub>2</sub>/hBN van der Waals heterostructure<sup>67</sup> (Fig. 6a). The luminescent WSe<sub>2</sub> layer is sandwiched between hBN layers with higher energy bandgaps. The diffusion length of electrons and holes in hBN is in the

micrometer range and the thickness of the heterojunction layer is tenths of micrometers. The electron can reach the WSe<sub>2</sub> layer before recombination to achieve electron injection (Fig. 6b). Optical microscope images and monochromatic CL images of the heterostructure are shown in Figs. 6c and 6d, from which the CL signal enhancement can be clearly observed. The same phenomenon is also observed in MoS<sub>2</sub> and WS<sub>2</sub> layers. Enhanced CL spectroscopy can be used to analyze strain-induced exciton peak shift in 2D semiconductor materials with this structure. This report paves the way for studying exciton recombination in the 2D material by CL microscopy. Heterostructures may have potential applications in high-energy particle detectors, field emission display technologies and transmission electron microscope displays.

### CL microscopy for metallic nanostructures

As the development of modern physics and nanofabrication techniques, plasmonics has matured significantly in the past few decades. The collective excitation of free electrons in metallic nanostructures, known as SPs, has been demonstrated to show fascinating optical properties like light localization, field enhancement and the improvement of LDOS, which greatly benefits the development of nanophotonics and finds applications in many areas including bio-sensing<sup>68</sup>, light harvesting and optical communications<sup>69</sup>. As the optical properties of metallic nanostructures crucially depend on the exploitation of plasmonic resonances, numerous light technologies and devices require precise knowledge of electromagnetic mode distributions, which directly determine the efficiency of light-matter interactions. Recently, CL micros-

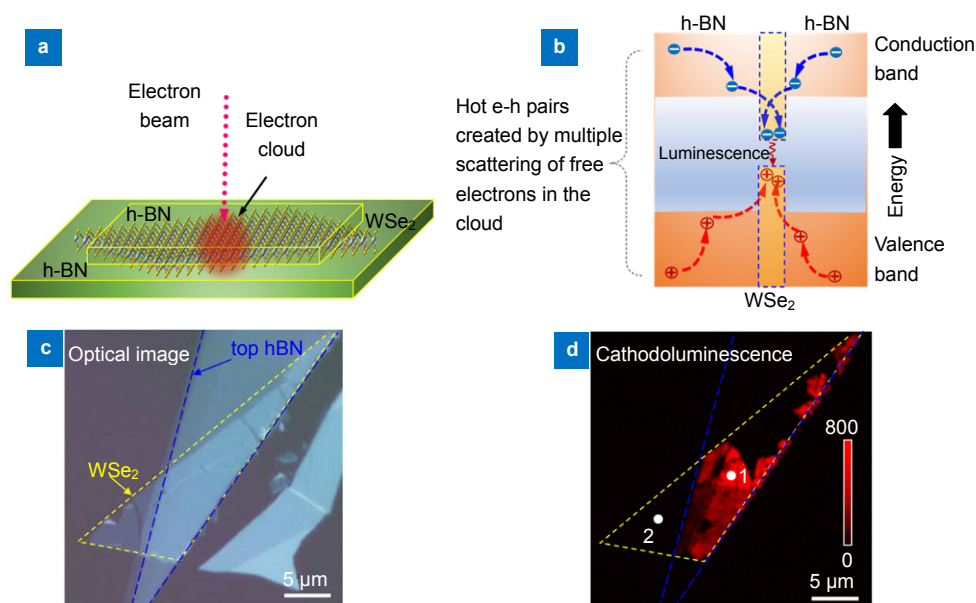


**Fig. 6** | (a) Schematic of hBN/WSe<sub>2</sub>/hBN van der Waals heterojunction excited by electron beam. (b) Process of the generation, diffusion, and recombination of electron–hole (e–h) pairs in heterojunction. (c) Optical microscope image of a hBN/WSe<sub>2</sub>/hBN heterostructure. (d) Monochromatic CL image of the heterostructure at WSe<sub>2</sub> emission energy (1.66 eV). Figure reproduced from ref. <sup>67</sup>, ACS Publications.

copy with nanoscale resolution was successfully used in the investigation of plasmonic modes in various nanostructures such as metallic nanoantennas<sup>70</sup> and photonic crystals<sup>71</sup>.

Under the electron beam stimulation, the CL signal can be generated from metallic nanostructures with the excitation of plasmonic modes, which is dominated by electron-induced radiation emission (EIRE). In this case, the induced electromagnetic field is coherent with the external evanescent field created by moving electrons. However, the radiative incoherent decay in metallic nanostructures only has a minor contribution to CL emissions, because the coherent electronic relaxation is several orders of magnitude faster. The scanning electron beam functions as a linear current source, enabling flexible mode excitation and control, and plasmonic mode distributions can be simultaneously probed with CL emissions.

Metallic nanostructures also provide a versatile platform for the manipulation of light-matter interactions. By utilizing the CL microscopy, the radiative LDOS distribution that governs the radiative spontaneous decay of quantum emitters, can be probed with deep-subwavelength resolution, facilitating the investigation of quantum optics. Moreover, various physical systems and devices can be exploited and manipulated at deep-subwavelength scale by using the CL microscopy, which can be used to find unrevealed physical phenomena such as the hidden chirality in achiral nanoantennas.

With the polarization-resolved and angle-resolved CL microscopy, the polarization state and radiation information in momentum space can be obtained, promoting the design of nanophotonic light emission devices. By exploiting the time-resolved function, the ultra-fast dynamics of quantum emission can be further acquired, which benefits the knowledge of underlying quantum physical principles.

Resolving the standing wave mode of a single nanoantenna is fundamental to further plasmonic research. Conventionally, optical excitation only weakly produces even-order modes under the off-normal excitation angle as illustrated in scattering spectrum<sup>42</sup> (Fig. 7a). By contrast, in CL spectroscopy, there are both odd and even-order modes indicated as  $l=3$ , and  $l=4$  (bottom spectra of Figs. 7b and 7c). Because electrons possess higher energy than light, higher-order modes are allowed to exist. As Figs. 7b and 7c show, CL emission intensity is proportional to the radiative LDOS. Furthermore, these two modes can be separated by adding bandpass filter in the collection optical path, which is easy to be achieved. The coupling structure of nanowires and nanoantennas (Fig. 7d) was discussed as well. Comparing two kinds of structures, it is shown that for the asymmetric mode, the total coupling efficiency is low and only the characteristics of its hybrid mode are preserved (Fig. 7e). It is possible to adjust the coupling efficiency of the hybrid mode by adjusting two arms of the nanowire, thereby affecting

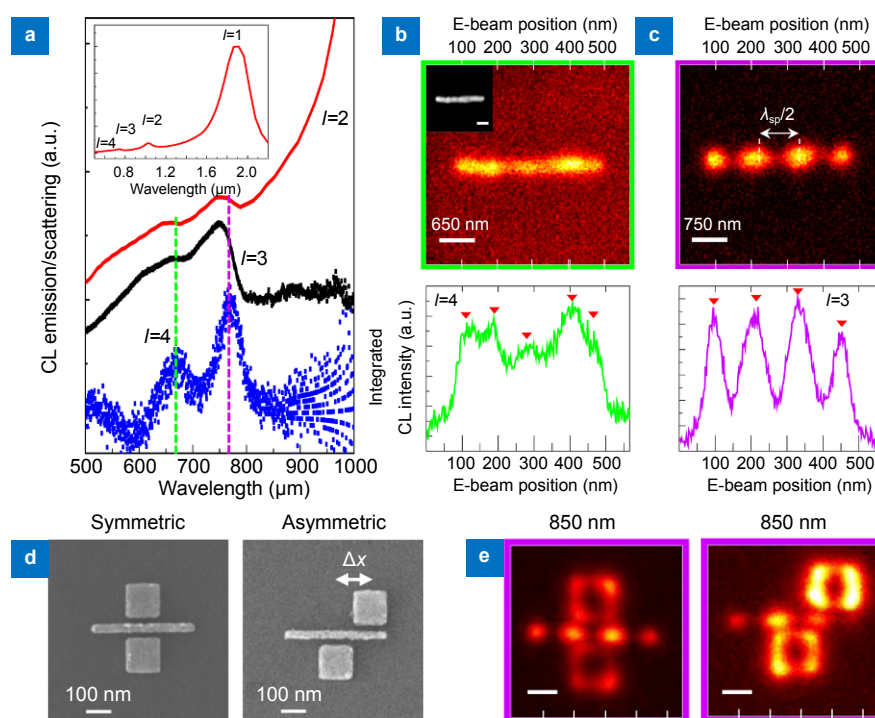


**Fig. 7** | (a) FDTD (red) simulated, dark-field (black) scattering and CL emission spectrum of Au antenna indicate the standing wave eigenmodes. CL images of nanoantenna with bandpass filter at (b) 650 nm and (c) 750 nm. Integrated CL intensity shows the standing wave plasmon resonances. (d) SEM images of symmetric and asymmetric coupling structure of nanowire and nanoantennas. (e) CL images of two coupling structures with bandpass filter at 850 nm. Figure reproduced from ref. <sup>42</sup>, ACS Publications.

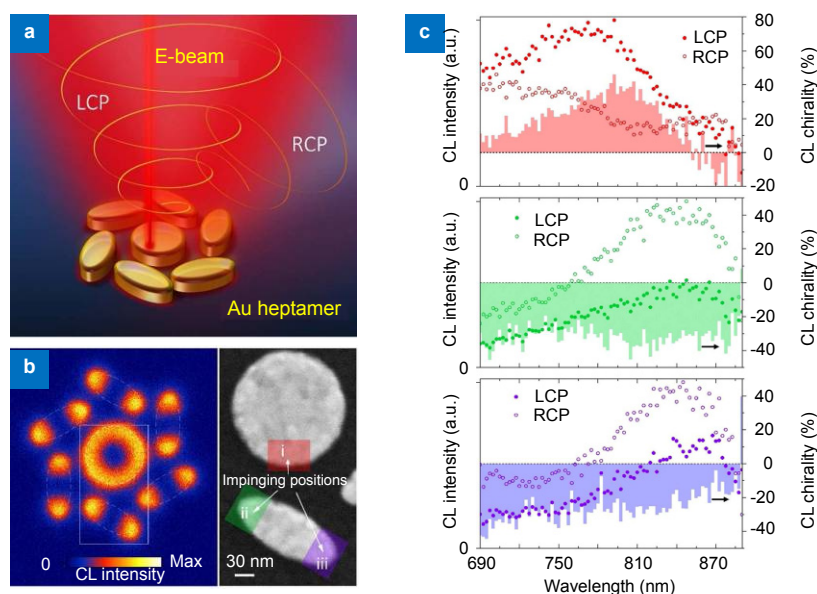


**Fig. 8** | (a) Schematic of the electron stimulated heptamer nanostructure. (b) Left: panchromatic CL image of Au heptamer nanostructures. Right: part of SEM image of Au heptamer. (c) CL spectra measured from impinging positions as indicated in (b). Figure reproduced from ref. <sup>72</sup>, ACS Publications.

the property of the nanowire plasmon. The near-field coupling reveals the influence of plasmon hybridization on the electron density of states of nanowire luminescence, the strong coupling between two structures here is due to the coincidence of the local plasmonic energy of the nanowire and the energy of the adjacent dipole of the nanoantenna. The CL technique enables the characterization of coupling properties at nanoscale, confirming the position according to SEM while performing LDOS analysis at any position.

The chiral light emission of nanoantennas is crucial to nanophotonics<sup>73</sup>. CL technology provides a favorable platform for the tuning of chiral at sub-nanoscale. Figure 8a shows an example of Au heptamer to produce a giant chiral CL response under electron beam excitation<sup>72</sup>. The corresponding chiral CL emission can be obtained by exciting different positions marked as i–iii (Fig. 8b) of the heptamer. Right-handed circularly polarized (RCP) and left-handed circularly polarized (LCP) CL contributions of the whole structure stimulated at different impinging positions have been observed. From measured CL spectra, the intensity of LCP CL collected under position i is larger than RCP CL. On the other side, opposite circular polarization emission states can be obtained by stimulating positions ii and iii (Fig. 8c). Furthermore, during the movement of the electron beam from point ii to point i, the switch of chirality occurs within 1.86 nm. According to this phenomenon, the ternary notation information coding was demonstrated at sub-nanoscale. This report opens the gate to further expansions of CL technology in quantum communication.

Except for resolving and manipulation, some phenomena hardly visible under optical excitation, like hidden chirality in achiral nanostructures, were discovered.

Due to the interference between symmetric and antisymmetric modes of the structure, the generated chirality of a symmetrical Al nanoantenna stimulated by the normal incident light, is hidden in the near field. Traditional optical characterization method is difficult to characterize the chirality effect in the near-field of the nanostructure. However, using circularly polarized resolved CL microscopy can reveal the hidden chirality of

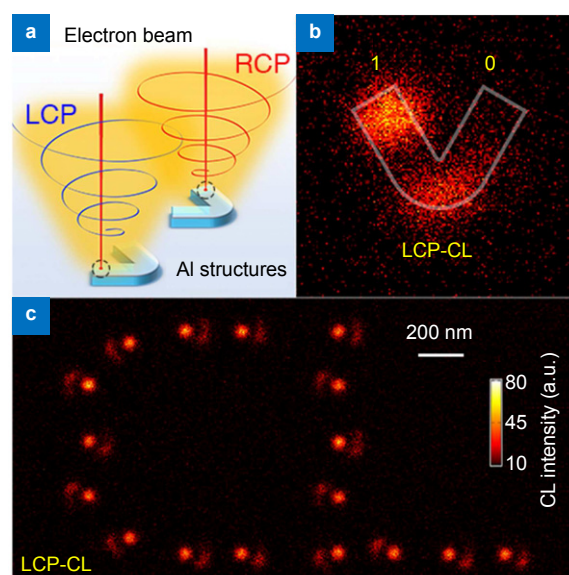


**Fig. 9** | (a) Schematic of circular polarization resolved Al nanoantenna with electron beam excitation. (b) LCP CL image of a single nanostructure with a bandpass of 657 nm. (c) LCP CL image for the helicity-dependent 2D display of capital letters “CL”. Figure reproduced from ref. <sup>74</sup>, ACS Publications.

the single symmetrical Al nanoantenna in the near-field<sup>74</sup> (Fig. 9a). The measured LCP or RCP CL, generated by stimulating arm-ends (left-arm or right-arm) with electron beam, can reflect the chiral radiative LDOS distribution. Therefore, the change of electron beam excitation position allows active switching of CL helicity at sub-nanoscale. Figure 9b shows that light and shade of arm-ends correspond to 0 or 1 known as binary encoding. In addition, these nanoantenna units can be used to design helicity-dependent coding arrays to achieve 2D display, as shown in Fig. 9c. This demonstration is expected to encourage CL microscopy applied in quantum information field.

The optical nanoantenna mediates the optical coupling between emitters and the far field for better light emission and reception. Exploring the response of the nanoantenna requires accurate positioning of the sub-wavelength scale transmitter with known orientation. Since the size of the nanoantenna is much smaller than the wavelength of light. The use of high-energy electron beam as the excitation source to study the emission characteristics of the Yagi-Uda antenna composed of Au nanoparticle arrays has been proposed<sup>75</sup>. It is inferred that the emission direction of nanoantennas depends on the near-field and far-field interaction of plasmonic resonance by collecting the angular resolution spectrum of nanoantennas at different wavelengths. When the left-most particle is excited by the electron beam, most of the CL is collected in a lobe pointing to the right of the antenna (Fig. 10). If taking the blue line in Fig. 10b as a cross-cut, the intensity and range size of left and right lobe can be obtained as shown in Fig. 10d. Furthermore, by moving the excitation point to detect the direction of nanoantennas at different wavelengths, the results show that emission characteristics vary with different wavelengths. The experimental result indicates that Au nanoparticles can be regarded as vertical dipoles perpendicular

to the substrate when they are excited by electron beams, which well explains the radiation pattern caused by the collective interference of light radiated by five coherently coupled dipole moments in nanoantennas. In conclusion, as a high-resolution technique, the angle-resolved CL spectroscopy can be effectively used to characterize the emission directivity of simple and even composite structures.

The radiative lifetime of nanoantenna is also concerned for plasmonic research. The introduction of ultra-fast pump detection technology to the CL microscopy technology enables the dynamic process detection of quantum phenomena such as charge transfer, quantum tunneling, simultaneously on the nanometer scale and the femtosecond time scale. The parabolic mirror is now used as a condenser to focus the femtosecond laser onto the sample and pump the electrons in the sample to the excited state. At the same time, using the femtosecond electron beam pulse generated by the same femtosecond laser as a probe to detect the sample, the relaxation of electrons in the sample can be obtained by controlling the time delay of the pump light and the detection electron beam. Time-resolved CL technology can record spectral changes at different time, show the instantaneous state and make up for the defect of integral spectrum. For example, time-resolved techniques provide a powerful means of studying effects of plating Au or Al layer on the surface of GaAs/AlAs/GaAs nanowires<sup>76</sup>. In this structure, high energy electron beam irradiation can generate excessive electron-hole pairs in the semiconductor nanostructure, excitons derived from the electron-hole pairs are coupled with SPs of the nanoantenna. In this process, time-resolved technology can directly measure the instantaneous carrier lifetime which changes with temperature (Fig. 11). Time-resolved technology is more real-time than the physical information reflected by the ordinary spectrum, which is an effective way to analyze

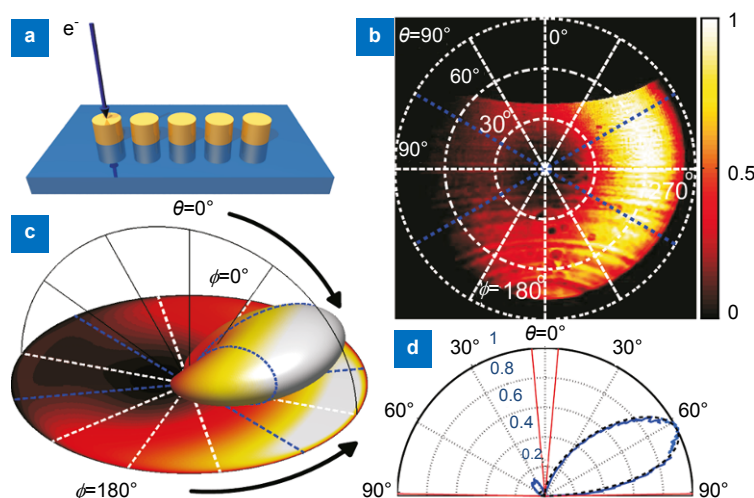


**Fig. 10** | (a) Schematic of the excitation geometry. (b) CL emission intensity as a function of angle. (c) 3D representation of theoretical radiation pattern for this excitation position and wavelength, together with a projection onto a 2D grid. (d) Cross-cut through the angular data showing CL intensity as a function of  $\theta$  (blue curve) together with theory (black dashed curve). Figure reproduced from ref. <sup>75</sup>, ACS Publications.

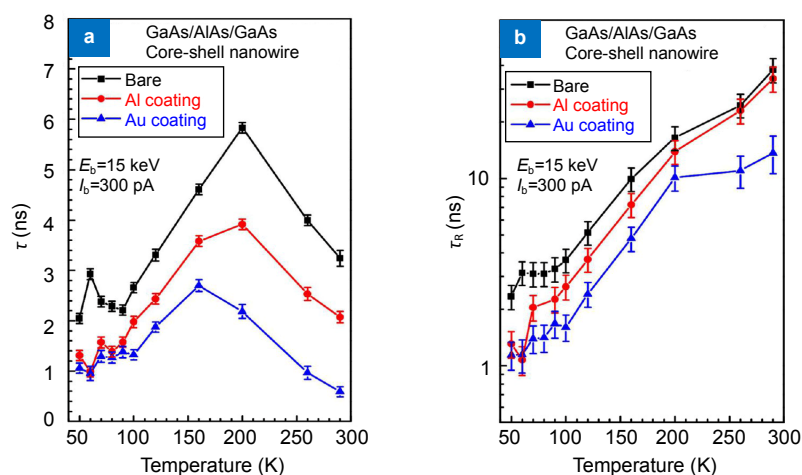


**Fig. 11 | Measured carrier decay times  $\tau(T)$  in (a) and radiative lifetime  $\tau_r(T)$  in (b) with time-resolved CL spectroscopy.** Figure reproduced from ref. <sup>76</sup>, ACS Publications.

the instantaneous light-emitting state of CL.

## Conclusions and outlook

In this paper, we mainly introduce advantages and applications of CL as a characterization tool in different materials system and physical perspectives. Based on the CL principle, some valuable information in the sample can be obtained, such as energy states of electrons and holes, plasmon behavior, carrier diffusion, exciton recombination kinetics. In the early development of semiconductors, CL technology can provide powerful support for the measurement of structural dislocations, carrier diffusion length, band structure and doping level in nanowires. With the flourishing development of micro-nano photonics and plasmonics, CL microscopy plays an essential role in the study of metallic nanostructures. It provides a technical guarantee for the visualization and the analysis of plasmon resonance modes. In addition to measuring peak wavelength and intensity-related information about the luminescence of a material, CL spectroscopy can also be used to obtain spatial distribution, polarization, time-domain information and angular distribution in combination with time-resolved and angle-resolved techniques.

Despite tremendous progress of CL microscopy, there are still many unresolved problems, such as weak CL signals and poor collection efficiency. According to correlative reports, utilizing additional fluorescence layer and system optimization can increase the CL intensity and improve the collection efficiency. With the increasing integration of equipments and samples, CL microscopy has continuously broadened its scope of applications, especially for semiconductors and metallic nanostructures. As an ultrahigh resolution imaging and analysis tool, CL microscopy provides direct guidelines for studying the physical mechanism of plasmonics in nanostructures. This can eventually promote practical applications in future optical circuits, quantum emitters and information fields.

## References

- Coenen T, Haegel N M. Cathodoluminescence for the 21st century: Learning more from light. *Appl Phys Rev* **4**, 031103 (2017).
- Pohl D W, Fischer U C, Dürig U T. Scanning near-field optical microscopy (Snom). *J Microsc* **152**, 853–861 (1988).
- Schieber J, Krinsley D, Riciputi L. Diagenetic origin of quartz silt in mudstones and implications for silica cycling. *Nature* **406**, 981–985 (2000).
- Pratesi G, Giudice A L, Vishnevsky S, Manfredotti C, Cipriani C. Cathodoluminescence investigations on the Popigai, Ries, and Lappajarvi impact diamonds. *Am Mineral* **88**, 1778–1787 (2003).
- Pennycook S J. Investigating the optical properties of dislocations by scanning transmission electron microscopy. *Scanning* **30**, 287–298 (2008).
- Watanabe K, Nagata T, Wakayama Y, Sekiguchi T, Erdélyi R *et al.* Band-Gap Deformation Potential and Elasticity Limit of Semiconductor Free-Standing Nanorods Characterized in Situ by Scanning Electron Microscope-Cathodoluminescence Nanospectroscopy. *ACS Nano* **9**, 2989–3001 (2015).
- Brenny B J M, Coenen T, Polman A. Quantifying coherent and incoherent cathodoluminescence in semiconductors and metals. *J Appl Phys* **115**, 244307 (2014).
- Storm K, Halvardsson F, Heurlin M, Lindgren D, Gustafsson A *et al.* Spatially resolved Hall effect measurement in a single semiconductor nanowire. *Nat Nanotechnol* **7**, 718–722 (2012).
- Niioka H, Furukawa T, Ichimiya M, Ashida M, Araki T *et al.* Multicolor Cathodoluminescence Microscopy for Biological Imaging with Nanophosphors. *Appl Phys Express* **4**, 112402 (2011).
- Barnett W A, Wise M L H, Jones E C. Cathodoluminescence of biological molecules, macromolecules and cells. *J Microsc* **105**, 299–303 (1975).
- Coenen T, Brenny B J M, Vesseur E J, Polman A. Cathodoluminescence microscopy: Optical imaging and spectroscopy with deep-subwavelength resolution. *MRS Bull* **40**, 359–365 (2015).
- Kociak M, Zagonel L F. Cathodoluminescence in the scanning transmission electron microscope. *Ultramicroscopy* **176**, 112–131 (2017).
- Gotze J. Potential of cathodoluminescence (CL) microscopy and spectroscopy for the analysis of minerals and materials. *Anal Bioanal Chem* **374**, 703–708 (2002).

14. Sauer R, Sternschulte H, Wahl S, Thonke K, Anthony T R. Revised fine splitting of excitons in diamond. *Phys Rev Lett* **84**, 4172–4175 (2000).
15. Koizumi S, Watanabe K, Hasegawa M, Kanda H. Ultraviolet emission from a diamond pn junction. *Science* **292**, 1899–1901 (2001).
16. Li G G, Geng D L, Shang M M, Peng C, Cheng Z Y *et al.* Tunable luminescence of Ce<sup>3+</sup>/Mn<sup>2+</sup>-coactivated Ca<sub>2</sub>Gd<sub>8</sub>(SiO<sub>4</sub>)<sub>6</sub>O<sub>2</sub> through energy transfer and modulation of excitation: potential single-phase white/yellow-emitting phosphors. *J Mater Chem* **21**, 13334 (2011).
17. Edwards P R, Martin R W. Cathodoluminescence nano-characterization of semiconductors. *Semicond Sci Tech* **26**, 064005 (2011).
18. Dierre B, Yuan X L, Sekiguchi T. Low-energy cathodoluminescence microscopy for the characterization of nanostructures. *Sci Technol Adv Mater* **11**, 043001 (2010).
19. Leto A, Pezzotti G. Cathodoluminescence study of off-stoichiometry and residual stresses in advanced dielectrics and related devices. *Phys Status Solidi A* **208**, 1119–1126 (2011).
20. Zhai T Y, Fang X S, Bando Y, Dierre B, Liu B D *et al.* Characterization, cathodoluminescence, and field-emission properties of morphology-tunable CdS micro/nanostructures. *Adv Funct Mater* **19**, 2423–2430 (2009).
21. Gautam U K, Panchakarla L S, Dierre B, Fang X S, Bando Y *et al.* Solvothermal Synthesis, Cathodoluminescence, and Field-Emission Properties of Pure and N-Doped ZnO Nanobullets. *Adv Funct Mater* **19**, 131–140 (2009).
22. Yacobi B G, Holt D B. Cathodoluminescence scanning electron microscopy of semiconductors. *J Appl Phys* **59**, R1–R24 (1986).
23. Shubina T V, Ivanov S V, Jmerik V N, Solnyshkov D D, Vekshin V A *et al.* Mie resonances, infrared emission, and the band gap of InN. *Phys Rev Lett* **92**, 117407 (2004).
24. Schue L, Berini B, Betz A C, Placais B, Ducastelle F *et al.* Dimensionality effects on the luminescence properties of hBN. *Nanoscale* **8**, 6986–6993 (2016).
25. Vesseur E J R, Aizpurua J, Coenen T, Reyes-Coronado A, Batsou P E *et al.* Plasmonic excitation and manipulation with an electron beam. *MRS Bull* **37**, 752–760 (2012).
26. Barnes W L, Dereux A, Ebbesen T W. Surface plasmon subwavelength optics. *Nature* **424**, 824–830 (2003).
27. Pendry J B, Martin-Moreno L, Garcia-Vidal F J. Mimicking surface plasmons with structured surfaces. *Science* **305**, 847–848 (2004).
28. Nelayah J, Kociak M, Stéphan O, García de Abajo F J, Tencé M *et al.* Mapping surface plasmons on a single metallic nanoparticle. *Nat Phys* **3**, 348–353 (2007).
29. Choi H, Pile D F P, Nam S, Bartal G, Zhang X. Compressing surface plasmons for nano-scale optical focusing. *Opt Express* **17**, 7519–7524 (2009).
30. Dionne J A, Sweatlock L A, Atwater H A, Polman A. Plasmon slot waveguides: Towards chip-scale propagation with subwavelength-scale localization. *Phys Rev B* **73**, 035407 (2006).
31. Yamamoto N, Bhunia S, Watanabe Y. Polarized cathodoluminescence study of InP nanowires by transmission electron microscopy. *Appl Phys Lett* **88**, 153106 (2006).
32. Vesseur E J R, Coenen T, Caglayan H, Engheta N, Polman A. Experimental verification of  $n=0$  structures for visible light. *Phys Rev Lett* **110**, 013902 (2013).
33. Narvaez A C, Weppelman I G C, Moerland R J, Liv N, Zonneville A C *et al.* Cathodoluminescence Microscopy of nanostructures on glass substrates. *Opt Express* **21**, 29968–29978 (2013).
34. Aubry A, Lei D Y, Fernandez-Dominguez A I, Sonnefraud Y, Maier S A *et al.* Plasmonic light-harvesting devices over the whole visible spectrum. *Nano Lett* **10**, 2574–2579 (2010).
35. Ropers C, Neacsu C C, Elsaesser T, Albrecht M, Raschke M B *et al.* Grating-coupling of surface plasmons onto metallic tips: a nanoconfined light source. *Nano Lett* **7**, 2784–2788 (2007).
36. Cao Q, Lalanne P. Negative role of surface plasmons in the transmission of metallic gratings with very narrow slits. *Phys Rev Lett* **88**, 057403 (2002).
37. Bashevov M V, Jonsson F, MacDonald K F, Chen Y, Zheludev N I. Hyperspectral imaging of plasmonic nanostructures with nanoscale resolution. *Opt Express* **15**, 11313–11320 (2007).
38. Vesseur E J R, de Waele R, Kuttge M, Polman A. Direct observation of plasmonic modes in Au nanowires using high-resolution cathodoluminescence spectroscopy. *Nano Lett* **7**, 2843–2846 (2007).
39. Kuttge M, de Abajo F J G, Polman A. Ultrasmall mode volume plasmonic nanodisk resonators. *Nano Lett* **10**, 1537–1541 (2010).
40. Hofmann C E, Vesseur E J R, Sweatlock L A, Lezec H J, de Abajo F J G *et al.* Plasmonic modes of annular nanoresonators imaged by spectrally resolved cathodoluminescence. *Nano Lett* **7**, 3612–3617 (2007).
41. Chaturvedi P, Hsu K H, Kumar A, Fung K H, Mabon J C *et al.* Imaging of plasmonic modes of silver nanoparticles using high-resolution cathodoluminescence spectroscopy. *ACS Nano* **3**, 2965–2974 (2009).
42. Day J K, Large N, Nordlander P, Halas N J. Standing wave plasmon modes interact in an antenna-coupled nanowire. *Nano Lett* **15**, 1324–1330 (2015).
43. Arango F B, Coenen T, Koenderink A F. Underpinning Hybridization Intuition for Complex Nanoantennas by Magnetolectric Quadrupolar Polarizability Retrieval. *ACS Photonics* **1**, 444–453 (2014).
44. Acar H, Coenen T, Polman A, Kuipers L K. Dispersive Ground Plane Core-Shell Type Optical Monopole Antennas Fabricated with Electron Beam Induced Deposition. *ACS Nano* **6**, 8226–8232 (2012).
45. Koh A L, Bao K, Khan I, Smith W E, Kothleitner G *et al.* Electron energy-loss spectroscopy (EELS) of surface plasmons in single silver nanoparticles and dimers: influence of beam damage and mapping of dark modes. *ACS Nano* **3**, 3015–3022 (2009).
46. Flauraud V, Bernasconi G D, Butet J, Alexander D T L, Martin O J F *et al.* Mode Coupling in Plasmonic Heterodimers Probed with Electron Energy Loss Spectroscopy. *ACS Nano* **11**, 3485–3495 (2017).
47. Sun Q, Ueno K, Yu H, Kubo A, Matsuo Y *et al.* Direct imaging of the near field and dynamics of surface plasmon resonance on gold nanostructures using photoemission electron microscopy. *Light-Sci Appl* **2**, e118–e118 (2013).
48. Sun Q, Yu H, Ueno K, Kubo A, Matsuo Y *et al.* Dissecting the Few-Femtosecond Dephasing Time of Dipole and Quadrupole Modes in Gold Nanoparticles Using Polarized Photoemission Electron Microscopy. *ACS Nano* **10**, 3835–3842 (2016).
49. Toth M, Phillips M R. Monte Carlo modeling of cathodoluminescence generation using electron energy loss curves. *Scanning* **20**, 425–432 (1998).
50. Titchmarsh J M, Booker G R, Harding W, Wight D R. Carrier recombination at dislocations in epitaxial gallium phosphide lay-

- ers. *J Mater Sci Mater Med* **12**, 341–346 (1977).
51. Nakagawa K, Maeda K, Takeuchi S. Observation of dislocations in cadmium telluride by cathodoluminescence microscopy. *Appl Phys Lett* **34**, 574 (1979).
  52. Zarem H A, Sercel P C, Lebens J A, Eng L E, Yariv A *et al.* Direct determination of the ambipolar diffusion length in GaAs/AlGaAs heterostructures by cathodoluminescence. *Appl Phys Lett* **55**, 1647–1649 (1989).
  53. Merano M, Sonderegger S, Crottini A, Collin S, Renucci P *et al.* Probing carrier dynamics in nanostructures by picosecond cathodoluminescence. *Nature* **438**, 479–482 (2005).
  54. Chen H L, Himwas C, Scaccabarozzi A, Rale P, Oehler F *et al.* Determination of n-Type Doping Level in Single GaAs Nanowires by Cathodoluminescence. *Nano Lett* **17**, 6667–6675 (2017).
  55. Kaganer V M, Sabelfeld K K, Brandt O. Piezoelectric field, exciton lifetime, and cathodoluminescence intensity at threading dislocations in GaN{0001}. *Appl Phys Lett* **112**, 122101 (2018).
  56. Pozina G, Ciechonski R, Bi Z X, Samuelson L, Monemar B. Dislocation related droop in InGaN/GaN light emitting diodes investigated via cathodoluminescence. *Appl Phys Lett* **107**, 251106 (2015).
  57. Jahn U, Miguel-Sánchez J, Flissikowski T, Grahn H T, Hey R *et al.* Carrier diffusion lengths in (In,Ga)(As,N)/GaAs quantum wells studied by spatially resolved cathodoluminescence. *Phys Status Solidi C* **3**, 627–630 (2006).
  58. Pauc N, Phillips M R, Aimez V, Drouin D. Carrier recombination near threading dislocations in GaN epilayers by low voltage cathodoluminescence. *Appl Phys Lett* **89**, 161905 (2006).
  59. Jahn U, Ristić J, Calleja E. Cathodoluminescence spectroscopy and imaging of GaN(Al,Ga)N nanocolumns containing quantum disks. *Appl Phys Lett* **90**, 161117 (2007).
  60. Li Z W, Li Y, Han T Y, Wang X L, Yu Y *et al.* Tailoring MoS<sub>2</sub> Exciton-Plasmon Interaction by Optical Spin-Orbit Coupling. *ACS Nano* **11**, 1165–1171 (2017).
  61. Li Z W, Xiao Y D, Gong Y J, Wang Z P, Kang Y M *et al.* Active light control of the MoS<sub>2</sub> monolayer exciton binding energy. *ACS Nano* **9**, 10158–10164 (2015).
  62. Zu S, Li B W, Gong Y J, Li Z W, Ajayan P M *et al.* Active control of plasmon-exciton coupling in MoS<sub>2</sub>-Ag hybrid nanostructures. *Adv Opt Mater* **4**, 1463–1469 (2016).
  63. Li Y, Li Z W, Chi C, Shan H Y, Zheng L S *et al.* Plasmonics of 2D Nanomaterials: Properties and Applications. *Adv Sci (Weinh)* **4**, 1600430 (2017).
  64. Li B W, Zu S, Zhou J D, Jiang Q, Du B W *et al.* Single-Nanoparticle Plasmonic Electro-optic Modulator Based on MoS<sub>2</sub> Monolayers. *ACS Nano* **11**, 9720–9727 (2017).
  65. Li Z W, Ye R Q, Feng R, Kang Y M, Zhu X *et al.* Graphene Quantum Dots Doping of MoS<sub>2</sub> Monolayers. *Adv Mater* **27**, 5235–5240 (2015).
  66. Kang Y M, Najmaei S, Liu Z, Bao Y J, Wang Y M *et al.* Plasmonic hot electron induced structural phase transition in a MoS<sub>2</sub> monolayer. *Adv Mater* **26**, 6467–6471 (2014).
  67. Zheng S J, So J K, Liu F C, Liu Z, Zheludev N *et al.* Giant Enhancement of Cathodoluminescence of Monolayer Transitional Metal Dichalcogenides Semiconductors. *Nano Lett* **17**, 6475–6480 (2017).
  68. Becker J, Trügler A, Jakab A, Hohenester U, Sönnichsen C. The Optimal Aspect Ratio of Gold Nanorods for Plasmonic Bio-sensing. *Plasmonics* **5**, 161–167 (2010).
  69. Jung K Y, Teixeira F L, Reano R M. Au/SiO<sub>2</sub> Nanoring Plasmon Waveguides at Optical Communication Band. *J Lightwave Technol* **25**, 2757–2765 (2007).
  70. Knight M W, Liu L F, Wang Y M, Brown L, Mukherjee S *et al.* Aluminum plasmonic nanoantennas. *Nano Lett* **12**, 6000–6004 (2012).
  71. Christ A, Tikhodeev S G, Gippius N A, Kuhl J, Giessen H. Waveguide-plasmon polaritons: strong coupling of photonic and electronic resonances in a metallic photonic crystal slab. *Phys Rev Lett* **91**, 183901 (2003).
  72. Han T Y, Zu S, Li Z W, Jiang M L, Zhu X *et al.* Reveal and Control of Chiral Cathodoluminescence at Subnanoscale. *Nano Lett* **18**, 567–572 (2018).
  73. Zu S, Bao Y J, Fang Z Y. Planar plasmonic chiral nanostructures. *Nanoscale* **8**, 3900–3905 (2016).
  74. Zu S, Han T, Jiang M, Lin F, Zhu X *et al.* Deep-Subwavelength Resolving and Manipulating of Hidden Chirality in Achiral Nanostructures. *ACS Nano* **12**, 3908–3916 (2018).
  75. Coenen T, Vesseur E J R, Polman A, Koenderink A F. Directional emission from plasmonic Yagi-Uda antennas probed by angle-resolved cathodoluminescence spectroscopy. *Nano Lett* **11**, 3779–3784 (2011).
  76. Estrin Y, Rich D H, Kretinin A V, Shtrikman H. Influence of metal deposition on exciton-surface plasmon polariton coupling in GaAs/AlAs/GaAs core-shell nanowires studied with time-resolved cathodoluminescence. *Nano Lett* **13**, 1602–1610 (2013).

## Acknowledgements

We are grateful for financial supports from the National Key Research and Development Program of China (Grant No. 2017YFA0205700), National Basic Research Program of China (Grant Nos. 2015CB932403 and 2017YFA0206000), National Science Foundation of China (Grant Nos. 11674012, 61422501, 11374023, 61521004, and 21790364), Foundation for the Author of National Excellent Doctoral Dissertation of PR China (Grant No. 201420), and National Program for Support of Top-notch Young Professionals (Grant No. W02070003).

## Author contributions

Z X Liu and M L Jiang contributed equally to this work. All authors commented on the manuscript.

## Competing interests

The authors declare no competing financial interests.